ChemPubSoc Europe
DOI: 10.1002/cphc.201700962
CHEMPHYSCHEM
Articles

VIP *Very Important Paper*

# Phase Equilibrium of $TiO_2$ Nanocrystals in Flame-Assisted Chemical Vapor Deposition

Changran Liu,[a] Joaquin Camacho,[b] and Hai Wang*[a]

Nano-scale titanium oxide ($TiO_2$) is a material useful for a wide range of applications. In a previous study, we showed that $TiO_2$ nanoparticles of both rutile and anatase crystal phases could be synthesized over the size range of 5 to 20 nm in flame-assisted chemical vapor deposition. Rutile was unexpectedly dominant in oxygen-lean synthesis conditions, whereas anatase is the preferred phase in oxygen-rich gases. The observation is in contrast to the 14 nm rutile–anatase crossover size derived from the existing crystal-phase equilibrium model. In the present work, we made additional measurements over a wider range of synthesis conditions; the results confirm the earlier observations. We propose an improved model for the surface energy that considers the role of oxygen desorption at high temperatures. The model successfully explains the observations made in the current and previous work. The current results provide a useful path to designing flame-assisted chemical vapor deposition of $TiO_2$ nanocrystals with controllable crystal phases.

## 1. Introduction

Flames offer an attractive chemical vapor deposition (CVD) route to nanostructure preparation. Well-designed flame environments can produce metal oxide nanoparticles and structures with high purity, high throughput rate, controllable size, crystal phase and morphology.[1–3] Examples include carbon nanoparticles[4], nanotubes,[5,6] flakes and needle arrays,[7] magnetite,[8] and nanoscale catalysts.[9] One of the frequently studied metal-oxides is titanium dioxide or titania ($TiO_2$). Rutile and anatase are two common polymorphs of $TiO_2$, and they differ notably in properties.[10,11] As a metastable form of titania,[12] anatase has garnered considerable interest owing to its wide ranging applications, from dye-sensitized solar cells[13] and photoelectric chemical catalysis[14] to chemical sensors.[15] Doped $TiO_2$ can exhibit rich electronic,[16] electrochemical,[17] catalytic[18] and photocatalytic[19,20] properties that are the basis of many emerging applications.

Studies of crystal phase stability and transformation in $TiO_2$ extend from the classical work on bulk $TiO_2$[21] to the more recent evaluations of nanoparticles.[22–25] Surface free energy plays an important role in crystal-phase equilibrium in nanoparticles and nanostructures. Notably, by considering the surface energy and surface stress of fully oxygenated $TiO_2$ surfaces, Banfield and co-workers[22,23,25] constructed a phase diagram for $TiO_2$ nanoparticles using results of atomistic simulation.[26] The rutile-anatase crossover diameter was predicted to be around 14 nm over the temperature range of 300 to 1000 K, below which anatase is thermodynamically favored.

A series of flame synthesis studies we conducted over the past years[13,27–29] suggest that the phase equilibrium of $TiO_2$ nanocrystals cannot be fully described by Banfield's model. Although the earlier results are not as conclusive owing to the limited range of gas conditions in which rutile was found to be dominant, these studies did show that rutile particles $<14$ nm and anatase particles $>14$ nm can be reproducibly prepared in flames.[13,27,28] The determining factor appears to be the gas-phase composition and more specifically, the availability of molecular oxygen. While anatase was the dominant crystal phase in oxygen-rich conditions, rutile was predominant in oxygen-deficient environment. Similar observations were reported in co-flow diffusion flames in which controlled quenching led to some degree of controlled titania nanoparticle crystal phase.[30,31]

The observations suggest that a more generalized thermodynamic interpretation is required to make useful predictions for the crystal phase of $TiO_2$ nanoparticles when they are prepared at high temperatures. The theory should probably consider the effect of oxygen desorption on surface energy and resolve the interplay among surface composition, surface energy, and crystal phase stability. Qualitative evidence about this interplay is abundant. Adsorption and passivation was found to have a considerable impact on the surface free energy, which, in turn, can influence the crystal shape.[32–34] Water at 100–300 °C passivates $TiO_2$ surfaces, an effect of which is to reduce the surface energy and the anatase-rutile crossover size.[24] The sensitivity of the crossover size to surface composition was also reported in thermal coarsening experiments.[35,36] Atomistic simulations revealed the sensitivity of

---

[a] *C. Liu, Prof. H. Wang*
*Mechanical Engineering Department*
*Stanford University*
*Stanford, CA 94305 (USA)*
*E-mail: haiwang@stanford.edu*

[b] *Prof. J. Camacho*
*Mechanical Engineering Department*
*San Diego State University*
*San Diego, CA 92189 (USA)*

The ORCID identification number(s) for the author(s) of this article can be found under https://doi.org/10.1002/cphc.201700962.

crossover size to surface H-atom bonding by showing that oxygenated surfaces and hydrated surfaces have different crossover sizes.[32,37] Calorimetry methods have provided insights into the contribution of oxygen desorption to phase equilibria of nano-crystalline metal oxide.[38,39] More recent calorimetry studies have considered the impact of grain boundaries[40,41] and particle shape[42] on crystal phase equilibria of titania nanocrystals.

The current study has two objectives. First, we provide conclusive evidence that rutile particles smaller than the crossover size of 14 nm and anatase particles larger than the crossover size can be prepared by simply manipulating the abundance of molecular oxygen in flames. Second, we propose a more generalized thermodynamic treatment for the phase stability of $TiO_2$ nanoparticles. The treatment supplements Banfield's model with a consideration of surface oxygen adsorption/desorption equilibrium.

## Experimental Methods

Titania nanoparticles are prepared using a flame CVD technique.[27,29,43] As illustrated in Figure 1, a quasi 1D disc-like gaseous flame sheet is stabilized at atmospheric pressure around 3 mm from a rotating surface. The mechanism of flame stabilization is flow stretch or anchoring of the flame due to gas flow divergence as it impinges against the surface. The reactant gas, issued through the nozzle, is combustible and comprised of ethylene, oxygen and argon. The gas is doped with vaporized titanium tetraisopropoxide (TTIP). $TiO_2$ nanoparticles nucleate in the flame sheet from Ti precursors and grow by particle coagulation and surface condensation/reaction. The temperature gradient in the particle growth region between the flame and the rotationally chilled surface can exceed 5000 K cm$^{-1}$, thus producing a strong thermophoretic force $F_T$ on the growing particles which transports them to the surface for deposition into films. In the flame and after nucleation, the particle growth time is typically several milliseconds.[29]

The $TiO_2$ particle size is controlled by the Ti precursor concentration. The TTIP concentration ranges from 100 to 3000 ppm in the reactant gas. The flames can be oxygen-rich or oxygen-lean, depending on the $O_2$ concentration in the reactant gas. The oxygen abundance may be characterized by the equivalence ratio $\phi$, defined as the ratio of the actual ethylene-to-oxygen ratio to the stoichiometric ethylene-to-oxygen ratio. Thus, $\phi<1$ corresponds to excess oxygen, while $\phi>1$ is oxygen deficient for fuel oxidation. The equilibrium $O_2$ concentration is indicative of the $O_2$ abundance in region where particles are synthesized. The value may be determined in an adiabatic and isobaric equilibrium calculation of the burned gas. Table lists the equilibrium $O_2$ mole fraction $x_{O2,eq}$ for each flame, along with the adiabatic flame temperature $T_{ad}$. The thermochemical properties of TTIP was taken from Buerger et al,[44] and those of other species from USC Mech II.[45] It is worthy noting that the actual peak temperature of the synthesis flame is lower than the adiabatic flame temperature because of heat loss to the rotating surface. For example, the actual temperature is around 2100 K for flame 1a, while the adiabatic flame temperature is 2354 K.[27]

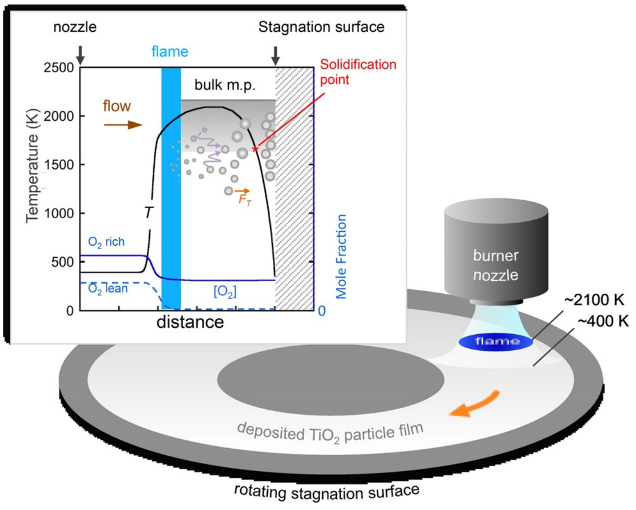

**Figure 1.** Schematic illustration of $TiO_2$ nanoparticle film preparation in a typical flame-assisted CVD setup.

Microscope slides are mounted flush to the rotating surface for particle collection. The deposited $TiO_2$ nanoparticle films are analyzed by X-ray diffraction (XRD) using PANalytical X'pert Pro diffractometer equipped with a Cu X-ray tube operating at 45 kV and 40 mA. The weight fraction of anatase and rutile was determined using the method of Spurr and Meyers.[46] The correction factor for the relatively high intensity of the [101] peak of anatase as compared to the rutile [110] peak was taken to be 0.842, an average of values reported previously.[22,46] The crystallite size is determined by fitting the peaks corresponding to the [211] face of rutile and the [101] face in anatase. A pseudo-Voigt function is used and the Scherrer's constant was taken for each face.[47]

Particles are examined under transmission electron microscopy (TEM, FEI Tecnai G2 F20 X-Twin at 200 keV) to confirm the XRD crystallite size and assess whether the spherical assumption applies. The samples are prepared by dispersing the particles by sonication in ethanol, followed by deposition onto a copper-supported holey carbon TEM grid (Electron Microscopy Sciences HC200-Cu) and drying. The particle size was determined from TEM images as the average of the major and minor axes of an ellipse drawn over each particle. The difference between the major and minor axis was typically within 10%.

## 2. Results and Discussion

The flame environment in which the nanoparticle synthesis takes place may be characterized by a rapid rise of the temperature close to the flame (see Figure 1), followed by a ≈2 mm region exceeding 2000 K. The particles nucleating from the gas-phase and in subsequent early growth stages are expected to be liquid-like droplets because the melting point of bulk $TiO_2$ is 2116 K and even lower for nanoparticles.[48–51] The particle-laden gas cools as the flow impinges on the chilled surface in the last 1 mm of reacting flow. During the thermophoretic transferring process, the particles cool and solidify into crystalline particles. The freezing temperature and gas composition at the solidification point are expected to determine the crystal phase of the particles eventually deposited onto the substrate. Although the freezing point of the particles is not precisely known and the particle ensemble effect causes different freezing points, our estimate is that the temperature at which this occurs is around 1800 K, as this may be inferred also from the MD results of Zhang et al.[51]

Six $TiO_2$ nanoparticle samples (OR1-3 and OL1-3) are prepared in the current work, as shown in Table 1. Along with six samples from a previous study,[27] they form the basis for the current analysis. The measured XRD crystallite size is listed in the same table for each sample. Typical XRD patterns of the deposited $TiO_2$ are shown in Figure 2. For particles prepared in oxygen-rich flames, the prominent (101) diffraction peak and the accompanying peaks are indicative of tetragonal anatase $TiO_2$. For oxygen-lean flames, prominent diffraction peaks, such as those corresponding to the (111) and (211) faces, are indicative of tetragonal rutile $TiO_2$. In all cases, there is a small contribution from anatase as indicated by the (101) peak. Again, for the oxygen lean conditions, the small diffraction peak at 33° could be due to the presence of $Ti_3O_5$, but its weight fraction is too small to be of importance to the present analysis.[52]

**Table 1.** Flame equivalence ratio ($\phi$), adiabatic temperature ($T_{ad}$), equilibrium $O_2$ mole fraction ($x_{O_2,eq}$), crystallite size and phase data of the $TiO_2$ particles synthesized.

| Flame | $\phi$ | $T_{ad}$ [K] | $x_{O_2,eq}$ | Crystallite size [nm][a] | %(wt) anatase[b] |
|---|---|---|---|---|---|
| OR1 | 0.44 | 2385 | $1.8\times10^{-1}$ | $<5$ | 78 |
| OR2 | 0.46 | 2329 | $1.5\times10^{-1}$ | 11.3 | 93 |
| OR3 | 0.59 | 2667 | $1.5\times10^{-1}$ | 17.7 | 94 |
| OL1 | 1.19 | 2557 | $3.3\times10^{-3}$ | $<5$ | 30 |
| OL2 | 1.15 | 2560 | $4.4\times10^{-3}$ | 7.5 | 26 |
| OL3 | 1.33 | 2606 | $1.7\times10^{-3}$ | 12.1 | 29 |
| 1a[c] | 0.52 | 2354 | $1.3\times10^{-1}$ | 11 | 91 |
| 1b[c] | 0.68 | 2551 | $8.5\times10^{-2}$ | 13 | 95 |
| 1c[c] | 0.83 | 2652 | $5.4\times10^{-2}$ | 13 | 71 |
| 2a[c] | 0.90 | 2651 | $3.7\times10^{-2}$ | 11 | 98 |
| 3a[c] | 1.13 | 2782 | $1.6\times10^{-2}$ | 8 | 20 |
| 4a[c] | 1.27 | 2797 | $9.3\times10^{-3}$ | 9 | 12 |

[a] as determined by XRD. [b] the balance is rutile. [c] taken from Memarzadeh et al.[27]

To verify the XRD crystallite site, we show in Figure 3 representative TEM images and size distribution for particles collected from the OR2 flame. In calculating the size distribution, the particles are assumed to be spherical using the TEM diameter values. The median diameter of the particle size distribution, 11.5 nm, is in close agreement with the XRD crystalline size at 11.3 nm. The particles synthesized are mostly single-crystal particles and XRD crystalline size is basically a measure of the particle size for even the less uniform particle compositions (e.g. the OL1 sample).

Figure 4 shows the weight percentage of anatase in the particle samples as a function of the crystallite size and equilibrium gas-phase $O_2$ mole fraction. The balance is the rutile fraction. While the top panel shows no correlation between the anatase fraction and crystallite size, the bottom panel displays the clear dependence of the crystal phase on gas-phase oxygen concentration. Anatase is the preferred phase when oxygen is abundant; rutile dominates the phase equilibrium when the oxygen concentration is low. The change from rutile dominance to anatase dominance occurs over a rather small range of $O_2$ concentrations. The results illustrate that the rutile

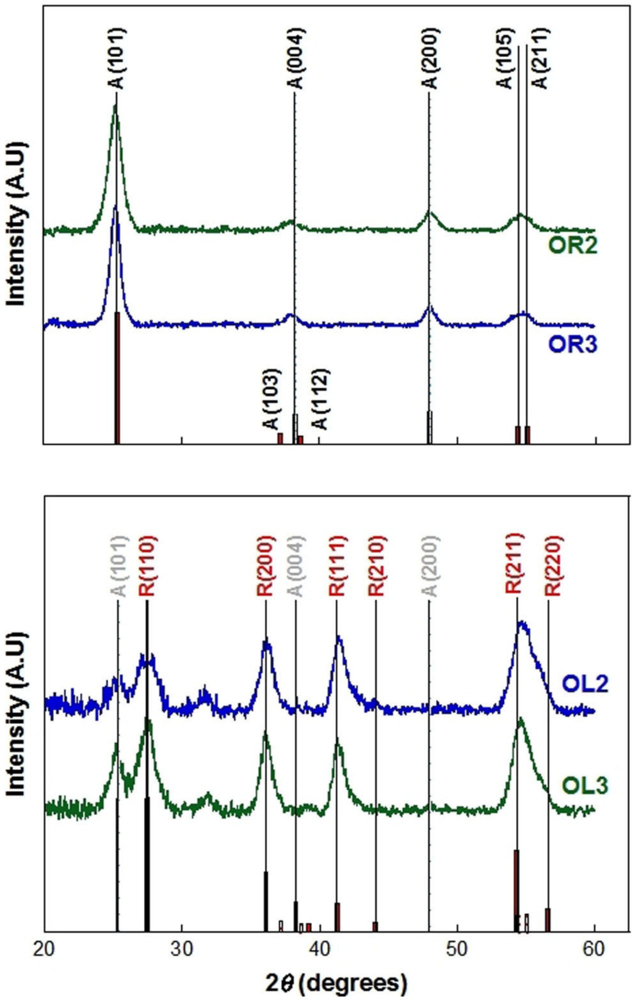

**Figure 2.** Selected XRD patterns of $TiO_2$ particles prepared in oxygen rich flames (top panel) and oxygen-lean flames (bottom panel).

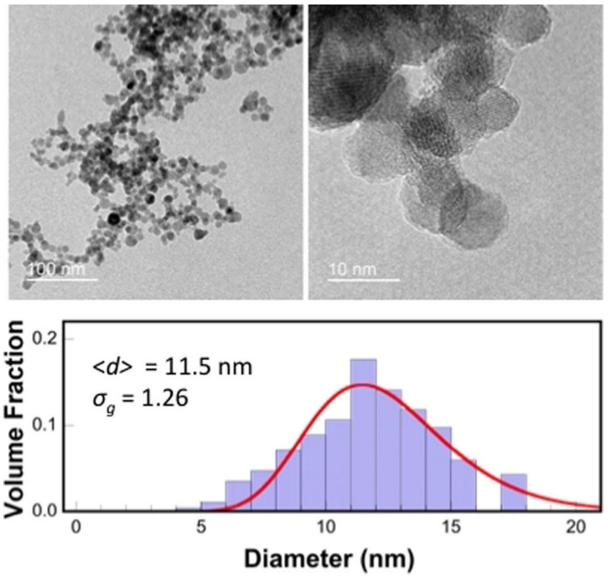

**Figure 3.** TEM images and volume distribution of OR2 particles. The histogram is collected from a sample of 239 particles. The fit to the size distribution uses the log-normal distribution.

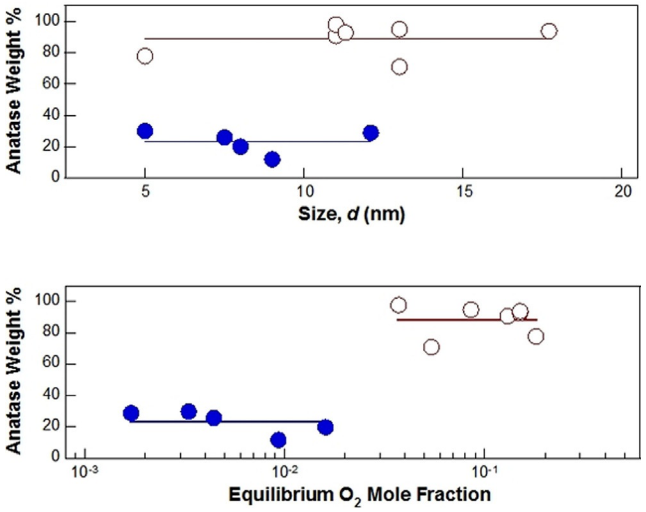

**Figure 4.** Anatase weight percent versus crystallite size (top panel) and equilibrium $O_2$ mole fraction (bottom panel). The balance is rutile. Symbols are experimental data: oxygen-lean: solid symbols; oxygen-rich: open symbols. Lines are drawn to guide the eyes.

crystal phase below 14 nm can be prepared at high temperatures so long as the system is deprived of oxygen at the point where particles solidify.

## 3. Modeling

The size dependence of the $TiO_2$ nanocrystal phase was explained in the spherical limit by Zhang and Banfield.[23] In their treatment, the Standard Gibbs free energy for anatase-to-rutile transformation is given as [Eq. (1)]:

$$\Delta G^\circ = \Delta_f G^\circ_R - \Delta_f G^\circ_A + 2(2t+3)\frac{M}{d}\left(\frac{\gamma_R}{\rho_R} - \frac{\gamma_A}{\rho_A}\right) = \begin{cases} > 0 & \text{anatase} \\ < 0 & \text{rutile} \end{cases} \qquad (1)$$

where subscripts R and A denote rutile and anatase, respectively, $\Delta_f G^\circ$ is the standard Gibbs energy of formation of the bulk-phase material, $t$ is the ratio of surface stress to surface free energy, $M$ is the molecular weight of $TiO_2$, $d$ is the crystallite size or particle diameter, $\gamma$ is the surface free energy, and $\rho$ is the mass density. According to [Eq. (1)], both bulk and surface properties impact the nano-$TiO_2$ phase stability. The surface effect increases as particle size decreases, thus causing the size dependence of the crystal phase equilibrium. Using the JANNAF thermodynamic properties[53] and the atomistic simulation result of surface energy of fully oxygenated $TiO_2$ surfaces,[26] [Eq. (1)] yields a crossover diameter of 14 nm below which anatase is more stable than rutile.

At high temperatures, oxygen desorption can be important to surface composition. For example, under oxygen-lean or reducing conditions, oxygen vacancy on bulk $TiO_2$ can be significant.[21,54] For a given temperature, the gas-phase oxygen concentration is the determining factor of the absorption/desorption equilibrium on $TiO_2$ surfaces.[12,43] Under oxygen deficient conditions, the reaction $2O^- \rightleftharpoons O_2(g) + 2s^-$ shifts to the right-hand side, leading to the formation of vacant sites $s^-$. In what follows, we demonstrate how surface oxygen vacancies can influence the surface energy and perturb the crystal phase equilibrium.

The oxygen desorption enthalpy $\Delta H^\circ_r$ at 298 K is reported to be 59 kcal mol$^{-1}$ for a mixture of anatase and rutile powder.[55] Earlier, we reported the desorption enthalpy to be 58 kcal mol$^{-1}$ for Degussa P25 nano-anatase (25 nm nominal diameter) and 54 kcal mol$^{-1}$ for 9-nm anatase particles prepared by the current flame CVD process.[43] The same $TiO_2$ nanoparticles show an $O_2$ desorption activation energy of $50.4 \pm 0.4$ kcal mol$^{-1}$ at 773 K.[43] The observed desorption enthalpy difference just discussed is consistent with recent findings that nanophase transition metal oxides show large thermodynamically driven shifts in oxidation-reduction equilibria.[38] That is, metal-oxygen bonds weaken toward small particle sizes.

Here, we use $\Delta H^\circ_{r,298K} = 55$ kcal mol$^{-1}$ to model the desorption enthalpy. The entropy and sensible enthalpy of $2O^-$ and $2s^-$ sites were assigned the values of $TiO_2$ and Ti, respectively. The vacant-site fraction $n_{s-}$ is obtained from the equilibrium constant $K_p$, [Eq. (2)]

$$K_p = \frac{P_{O_2}}{P^0}\left(\frac{n_{s-}}{1-n_{s-}}\right)^2 = e^{-\Delta G^\circ_{\text{anatase}\rightarrow\text{rutile}}(T)/RT} \qquad (2)$$

where $P^0$ is the standard pressure. For the current flame CVD process, $P_{O_2}/P^0$ is the gas-phase $O_2$ mole fraction $x_{O_2}$. The vacant-site fraction is therefore [Eq. (3)]:

$$n_{s^-} = \frac{\sqrt{K_p/x_{O_2}}}{1+\sqrt{K_p/x_{O_2}}} \qquad (3)$$

For $x_{O_2} < 10^{-2}$, which corresponds to an oxygen lean condition (see Table 1), we find that $n_{s-} > 36\,\%$ at 1500 K.

Equation (1) may be adapted to account for the influence of desorbed surface sites [Eq. (4)]:

$$\Delta G^\circ_{\text{anatase}\rightarrow\text{rutile}} = \Delta_f G^\circ_R - \Delta_f G^\circ_A + 2(2t+3)\frac{M}{d}\left(\frac{\gamma_{R/Ti}}{\rho_R} - \frac{\gamma_{A/Ti}}{\rho_A}\right) \qquad (4)$$

where $\gamma_{R/Ti}$ and $\gamma_{A/Ti}$ are the surface free energies of rutile and anatase with partially desorbed surfaces, respectively. These free energies may be estimated by [Eq. (5a) and (5b)]

$$\gamma_{R/Ti} = n_{s-}\gamma_{Ti} + \left(1-n_{s-}\right)\gamma_R \qquad (5a)$$

$$\gamma_{A/Ti} = n_{s-}\gamma_{Ti} + \left(1-n_{s-}\right)\gamma_A \qquad (5b)$$

In the above equations, $\gamma_{Ti}$ is the surface free energy of titanium. $\gamma_R$ and $\gamma_A$ may be calculated from [Eq. (6)]:

$$\gamma(T) = h(T) - Ts^{O}(T) = \left[h(0\mathrm{K}) + \int_0^T c(T)\mathrm{d}T\right] - T\int_0^T \frac{c(T)}{T}\mathrm{d}T \tag{6}$$

where $h(0\ \mathrm{K})$ is the surface enthalpy: $h_R(0\ \mathrm{K}) = 1.93\ \mathrm{J\,m^{-2}}$ and $h_A(0\ \mathrm{K}) = 1.34\ \mathrm{J\,m^{-2}}$.[23] The specific heat $c(T)$ may be estimated by extrapolation with the Debye theory[56] from the low-temperature measurement.[57] Using a Debye temperature value of 670 K for $TiO_2$,[58] we find $c = 2.12$, 2.30, and $2.33 \times 10^{-4}\ \mathrm{J\,m^{-2}K^{-1}}$ for $T = 500$, 1000, and 1500 K, respectively.

The surface free energy of titanium was assumed to be equal to that of its liquid phase[59] [Eq. (7)]

$$\gamma(\mathrm{J\,m^{-2}}) = 1.64 - 2.38 \times 10^{-4}[T - 1043] \tag{7}$$

where $T$ is in K. The ratio of solid-to-liquid surface specific heat was taken to be 1.18.[60] The thermal expansion was considered by treating the density $\rho$ as a function of temperature. $\rho$ decreases by $\approx 5\%$ as temperature increases from 300 to 2000 K.

The Gibbs free energy of bulk rutile and anatase were taken from the JANAF table [47], which may be parameterized as a function of $T$ (in K) from 300 to 2000 K as [Eq. (8) and (9)]:

$$\Delta_f G_R^\circ(\mathrm{J/mol}) = -9.46 \times 10^5 + 2.472 \times 10^2\, T - 9.593\, T \ln T + 2.994 \times 10^{-3}\, T^2 - 3.472 \times 10^5\, T^{-1} \tag{8}$$

$$\Delta_f G_A^\circ(\mathrm{J/mol}) = -9.41 \times 10^5 + 2.655 \times 10^2\, T - 12.21\, T \ln T + 3.966 \times 10^{-3}\, T^2 - 2.603 \times 10^5\, T^{-1} \tag{9}$$

Assuming $t = 1$,[23] the phase equilibrium may be calculated as a function of crystallite size (or particle diameter), gas-phase $O_2$ mole fraction $x_{O_2}$, and temperature $T$. Figure 5 shows the $\Delta G^\circ_{\mathrm{anatase}\rightarrow\mathrm{rutile}} = 0$ isosurface at 1 bar pressure. At low temperatures ($< 500$ K), oxygen desorption is unimportant, and the crossover size remains to be 14 nm. Above 500 K, oxygen desorption starts to impact the phase equilibrium, which generally leads to a reduction in the crossover size. Desorption of surface oxygen creates bare Ti sites, thus diminishing the effect of rutile and anatase specific surface free energy on the total Gibbs energy.

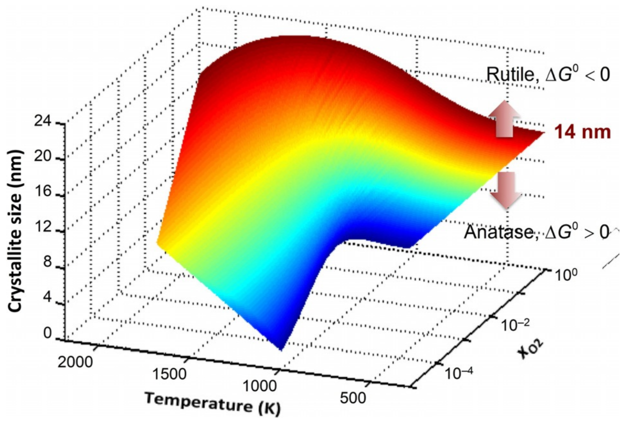

**Figure 5.** The $\Delta G^\circ_{\mathrm{anatase}\rightarrow\mathrm{rutile}} = 0$ isosurface dividing the rutile- and anatase-favored regimes, as a function of crystallite size, temperature and gas-phase $O_2$ mole fraction. The surface is applicable to 1 bar total pressure.

The $\Delta G^\circ_{\mathrm{anatase}\rightarrow\mathrm{rutile}} = 0$ iso-lines at three representative temperatures are plotted in Figure 6 along with experimental data. For each temperature shown, the region to the right of the line is predicted to be anatase and rutile is to the left of the line. It is seen that anatase is thermodynamically favored at high gas-phase $O_2$ concentrations and small particle sizes. In comparison, rutile can be preferred at small sizes as the oxygen concentration decreases. As mentioned earlier, the actual flame $O_2$ mole fraction is somewhat higher than the adiabatic equilibrium value because of heat loss and recombination below the adiabatic flame temperature. The difference, however, is expected to be small. It can be seen that the 1800 K iso-line divides the observed rutile-favored and anatase-favored conditions rather well. If the crystal phase of the particles is determined largely by the thermodynamic state at the point of solidification, the current result suggests the melting point of the $TiO_2$ nanoparticles to be around 1800 K, which is consistent with the result from a recent molecular dynamics simulation.[51]

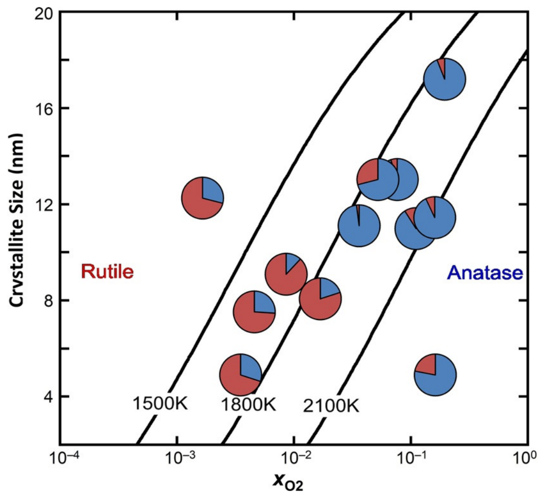

**Figure 6.** The $\Delta G^\circ_{\mathrm{anatase}\rightarrow\mathrm{rutile}} = 0$ isolines at several temperatures. The experimental data are shown as the pie symbols in which the blue fraction indicates measured anatase weight percentage, and the red fraction represents rutile fraction.

Lastly, we note that several other factors may influence the rutile-vs.-anatase fractions. The presence of other burned gases in the particle growth region could impact oxygen adsorption/desorption equilibrium especially for the oxygen-rich flames, where reducing gases such as CO and $H_2$ can have appreciable concentrations. The presence of these gas molecules should push the equilibrium to a further desorbed state, thus potentially reducing the crossover size even more. The finite width of the particle size distribution and the size dependence of the melting point present a new layer of complications. Additionally, kinetic factors, including the particle-cooling rate and the crystal-phase transformation of solidified particles, can also play a role in the crystal phase of the particles collected. Fast cooling causes the crystal phase to be frozen in a particular thermodynamic state; and this has been an underlying assumption of the current analysis. Subsequent solid-phase phase transformation is not expected to be significant as the particles are transported to the cooled surface over a time scale of merely $\approx 1$ ms. In any event, these kinetic effects are difficult to assess, especially for an ensemble of particles with varying sizes as the cooling rate and solid-phase transformation depend on the temperature-time history of a particle, and its size and melting point.

## 4. Conclusions

In this work, we conclusively demonstrated that rutile $TiO_2$ particles smaller than the traditionally accepted crossover size of 14 nm can be prepared in flame-assisted chemical vapor deposition. A thermodynamic analysis shows that in high-temperature vapor-phase synthesis, nano-$TiO_2$ crystal phase is determined strongly by the gas-phase oxygen concentration, and to a less extent by the particle or crystallite size. It is identified that oxygen desorption at high temperatures plays a critical role in the surface free energy, which, in turn, impacts the crystal phase equilibrium. The thermodynamic theory advanced by Banfield and workers has thus been extended to high-temperature conditions including the effect of oxygen adsorption/desorption on crystal phase equilibrium.

A more complete understanding emerges in terms of controlling the crystallite size and polymorph of $TiO_2$ nanoparticles in high-temperature, vapor-phase synthesis. Specifically, the flame temperature must be kept at a value higher than the melting point of the particles so that the growth of the particles by coagulation and surface condensation occurs while the particles are in the liquid phase. Under this condition, particles coalesce rather than aggregate as they grow in size. As the droplets are transported away from the high-temperature region toward a cold deposition surface, they solidify in the gas phase at some point. The crystal phase is determined largely by the gas-phase conditions at the point of solidification: particles exposed to an oxygen-rich environment turn to anatase, and those in an oxygen-depleted gas solidify to rutile.

## *Acknowledgements*

*The authors wish to thank Mr. Ruxiao An for helpful discussions. The work was supported by US Air Force of Scientific Research (AFOSR) under contract number FA9550-16-1-0486.*

## Conflict of interest

*The authors declare no conflict of interest.*

**Keywords:** chemical vapor deposition · crystal phase · metal oxide · nanoparticles · phase equilibrium

[1] H. K. Kammler, L. Mädler, S. E. Pratsinis, *Chem. Eng. Technol.* **2001**, *24*, 583 – 596.
[2] M. T. Swihart, *Curr. Opin. Colloid Interface Sci.* **2003**, *8*, 127 – 133.
[3] H. Wang, *Proc. Combust. Inst.* **2011**, *33*, 41 – 67.
[4] M. Schenk, S. Lieb, H. Vieker, A. Beyer, A. Gölzhäuser, H. Wang, K. Kohse-Höinghaus, *ChemPhysChem* **2013**, *14*, 3248 – 3254.
[5] L. Yuan, K. Saito, W. Hu, Z. Chen, *Chem. Phys. Lett.* **2001**, *346*, 23 – 28.
[6] R. L. Vander Wal, *Chem. Phys. Lett.* **2000**, *324*, 217 – 223.
[7] P. M. Rao, X. Zheng, *Nano Lett.* **2009**, *9*, 3001 – 3006.
[8] B. M. Kumfer, K. Shinoda, B. Jeyadevan, I. M. Kennedy, *J. Aerosol Sci.* **2010**, *41*, 257 – 265.
[9] R. Strobel, A. Baiker, S. E. Pratsinis, *Adv. Powder Technology* **2006**, *17*, 457 – 480.
[10] C. Di Valentin, G. Pacchioni, A. Selloni, *Phys. Rev. B* **2004**, *70*, 085116.
[11] U. Diebold, *Surf. Sci. Rep.* **2003**, *48*, 53 – 229.
[12] R. D. Shannon, J. A. Pask, *J. Am. Ceram. Soc.* **1965**, *48*, 391 – 398.
[13] S. Nikraz, H. Wang, *Proc. Combust. Inst.* **2013**, *34*, 2171 – 2178.
[14] P. Periyat, B. Naufal, S. G. Ullattil, *Mater. Sci. Forum* **2016**, *855*, 78 – 93.
[15] J. Bai, B. Zhou, *Chem. Rev.* **2014**, *114*, 10131 – 10176.
[16] M. M. Islam, T. Bredow, A. Gerson, *ChemPhysChem* **2011**, *12*, 3467 – 3473.
[17] T. Berger, D. Monllor-Satoca, M. Jankulovska, T. Lana-Villarreal, R. Gómez, *ChemPhysChem* **2012**, *13*, 2824 – 2875.
[18] F. Niu, S. Li, Y. Zong, Q. Yao, *J. Phys. Chem. C* **2014**, *118*, 19165 – 19171.
[19] N. Sakai, T. Ikeda, T. Teranishi, T. Tatsuma, *ChemPhysChem* **2011**, *12*, 2415 – 2418.
[20] N. Prakash, R. Karthikeyan, D. Thangaraju, M. Navaneethan, M. Arivanandhan, T. Koyama, Y. Hayakawa, *ChemPhysChem* **2015**, *16*, 3084 – 3092.
[21] K. J. D. MacKenzie, *Trans. J. Br. Ceram. Soc.* **1975**, *74*, 121 – 125.
[22] A. A. Gribb, J. F. Banfield, *Am. Mineral.* **1997**, *82*, 717 – 728.
[23] H. Zhang, J. F. Banfield, *J. Mater. Chem.* **1998**, *8*, 2073 – 2076.
[24] J. F. Banfield, H. Zhang, *Rev. Mineral. Geochem.* **2001**, *44*, 1 – 58.
[25] H. Zhang, J. F. Banfield, *Chem. Rev.* **2014**, *114*, 9613 – 9644.
[26] P. M. Oliver, G. W. Watson, E. Toby Kelsey, S. C. Parker, *J. Mater. Chem.* **1997**, *7*, 563 – 568.
[27] S. Memarzadeh, E. D. Tolmachoff, D. J. Phares, H. Wang, *Proc. Combust. Inst.* **2011**, *33*, 1917 – 1924.
[28] S. Nikraz, D. J. Phares, H. Wang, *J. Phys. Chem. C* **2012**, *116*, 5342 – 5351.
[29] E. D. Tolmachoff, A. D. Abid, D. J. Phares, C. S. Campbell, H. Wang, *Proc. Combust. Inst.* **2009**, *32*, 1839 – 1845.
[30] K. Wegner, S. E. Pratsinis, *AIChE J.* **2003**, *49*, 1667 – 1675.
[31] A. Teleki, S. E. Pratsinis, *Phys. Chem. Chem. Phys.* **2009**, *11*, 3742 – 3747.
[32] A. S. Barnard, P. Zapol, *Phys. Rev. B* **2004**, *70*, 235403.
[33] A. S. Barnard, P. Zapol, *J. Chem. Phys.* **2004**, *121*, 4276 – 4283.
[34] A. S. Barnard, P. Zapol, *J. Phys. Chem. B* **2004**, *108*, 18435 – 18440.
[35] J. R. McCormick, B. Zhao, S. A. Rykov, H. Wang, J. G. Chen, *J. Phys. Chem. B* **2004**, *108*, 17398 – 17402.
[36] T. B. Ghosh, S. Dhabal, A. K. Datta, *J. Appl. Phys.* **2003**, *94*, 4577 – 4582.
[37] A. S. Barnard, L. A. Curtiss, *Nano Lett.* **2005**, *5*, 1261 – 1266.
[38] A. Navrotsky, C. Ma, K. Lilova, N. Birkner, *Science* **2010**, *330*, 199 – 201.
[39] M. R. Ranade, A. Navrotsky, H. Z. Zhang, J. F. Banfield, S. H. Elder, A. Zaban, P. H. Borse, S. K. Kulkarni, G. S. Doran, H. J. Whitfield, *Proc. Natl. Acad. Sci. USA* **2002**, *99*, 6476 – 6481.
[40] R. H. R. Castro, B. Wang, *J. Am. Ceram. Soc.* **2011**, *94*, 918 – 924.
[41] R. H. R. Castro, *Mater. Lett.* **2013**, *96*, 45 – 56.
[42] T.-J. Park, A. A. Levchenko, H. Zhou, S. S. Wong, A. Navrotsky, *J. Mater. Chem.* **2010**, *20*, 8639 – 8645.
[43] E. Tolmachoff, S. Memarzadeh, H. Wang, *J. Phys. Chem. C* **2011**, *115*, 21620 – 21628.
[44] P. Buerger, D. Nurkowski, J. Akroyd, S. Mosbach, M. Kraft, *J. Phys. Chem. A* **2015**, *119*, 8376 – 8387.
[45] H. Wang, X. You, A. V. Joshi, S. G. Davis, A. Laskin, F. Egolfopoulos, C. K. Law, http://ignis.usc.edu/USC Mech II.htm **2007**.
[46] R. A. Spurr, H. Myers, *Anal. Chem.* **1957**, *29*, 760 – 762.
[47] J. I. Langford, A. J. C. Wilson, *J. Appl. Crystallogr.* **1978**, *11*, 102 – 113.
[48] C. Wronski, *British Journal of Applied Physics* **1967**, *18*, 1731.
[49] K. Dick, T. Dhanasekaran, Z. Zhang, D. Meisel, *J. Am. Chem. Soc.* **2002**, *124*, 2312 – 2317.
[50] K. Nanda, *Pramana* **2009**, *72*, 617.
[51] Y. Zhang, S. Li, W. Yan, S. D. Tse, *J. Appl. Phys.* **2012**, *111*, 124321.

[52] K. Fujiwara, Y. Deligiannakis, C. G. Skoutelis, S. E. Pratsinis, *Appl. Catal. B* **2014**, *154*, 9–15.
[53] M. W. Chase, Jr., C. A. Davies, J. R. Downey, D. J. Frurip, R. A. McDonald, A. N. Syverud, *J. Phys. Chem. Ref. Data* **1985**, *14*, Supplemental No. 1.
[54] R. D. Shannon, *J. Appl. Phys.* **1964**, *35*, 3414–3416.
[55] B. Halpern, J. E. Germain, *J. Catal.* **1975**, *37*, 44–56.
[56] P. Debye, *Ann. Phys.* **1912**, *39*, 789.
[57] J. Dugdale, J. Morrison, D. Patterson, P. Roy, *Soc. A-Math. Phys.* **1954**, *224*, 228.
[58] H. J. McDonald, H. Seltz, *J. Am. Chem. Soc.* **1939**, *61*, 2405–2407.
[59] K. Zhou, H. Wang, J. Chang, B. Wei, *Chem. Phys. Lett.* **2015**, *639*, 105–108.
[60] W. Tyson, W. Miller, *Surf. Sci.* **1977**, *62*, 267–276.

Manuscript received: August 29, 2017
Revised manuscript received: October 19, 2017
Accepted manuscript online: October 23, 2017
Version of record online: December 21, 2017